



TECHNICAL ARTICLE

Improving Productivity in the Laser Powder Bed Fusion of Inconel 718 by Increasing Layer Thickness: Effects on Mechanical Behavior

Paul Paradise, Dhiraj Patil, Nicole Van Handel, Samuel Temes, Anushree Saxena, Daniel Bruce, Austin Suder, Shawn Clonts, Mandar Shinde, Cameron Noe, Donald Godfrey, Rakesh Hota, and Dhruv Bhate

Submitted: 15 September 2021 / Revised: 24 March 2022 / Accepted: 18 April 2022 / Published online: 9 May 2022

Build time is a critical contributor to overall part cost in the Laser Powder Bed Fusion (L-PBF) process, which in turn plays an important role in whether a part is made with this process or not. While there are many ways to improve productivity in the L-PBF process, this work focuses on one specific approach in the context of L-PBF of Inconel 718: increasing layer thickness, which reduces the number of slices for a given part, but is accompanied with the potential for a degradation in mechanical properties. The study is separated into two parts: the first establishes an optimal process at each of three different layer thicknesses (30, 60 and 80 μm). Having developed an optimum process, the study then obtains density, surface roughness and mechanical property data on specimens fabricated with the selected processes, along with SEM micrographs. Half the specimens are characterized and tested in the as-built condition, the other half go through a heat treatment process that includes Hot Isostatic Pressing (HIP). This study of a total of 600 specimens across six builds confirms that an increase in layer thickness has no significant effect on elastic modulus, but does show reductions in density and strength, along with slight increases in surface roughness. Microstructural studies show no significant differences in grain size and orientation, with a slight increase in carbides and delta precipitates with increasing thickness. Post-heat treatment mechanical strength for all thicknesses is comparable to forged values for Inconel 718, and limited data suggest improvements in excess of forged values can be obtained if specimens are machined prior to testing, with a narrowing of the differences attributable to layer thickness. This study also showed correlations between strength and density and revealed build location dependence for UTS.

Keywords as-printed, build rate, HIP, Inconel 718, laser powder bed fusion, layer thickness, mechanical properties, productivity, throughput

1. Introduction

The ability to manufacture complex geometries with metal Additive Manufacturing (AM) processes such as Laser Powder Bed Fusion (L-PBF) has opened new opportunities for designers, manufacturers and engineers, particularly in the

This invited article is part of a special issue in the *Journal of Materials Engineering and Performance* entitled “Space and Aerospace Exploration Revolution: Metal Additive Manufacturing.” The issue was organized by Shahrooz Nafisi, Relativity Space; Paul Gradl, NASA Marshall Space Flight Center; Douglas Hofmann, NASA Jet Propulsion Laboratory/California Institute of Technology; and Reza Ghomashchi, The University of Adelaide, Australia.

Paul Paradise, Dhiraj Patil, Nicole Van Handel, Samuel Temes, Anushree Saxena, Daniel Bruce, Austin Suder, Shawn Clonts, Mandar Shinde, Cameron Noe, and Dhruv Bhate, 3DX Research Group, Arizona State University, Mesa, AZ 85212; **Donald Godfrey**, SLM Solutions Americas, Wixom, MI 48393; **Rakesh Hota**, Honeywell Aerospace, Phoenix, AZ 85034. Contact e-mail: dpbhate@asu.edu.

biomedical and aerospace industries (Ref 1). A key challenge to the wider adoption of L-PBF, however, is the cost of producing parts, in particular when they are intended for volume production. While there are different cost drivers for an AM made production part, a key factor is the cost of the machine itself, often captured in product costs as a depreciation factor, and the associated operation costs of running the machine (Ref 2). Each of these in turn is a function of build time, with faster build rates typically resulting in lower per-part cost. Several build time reduction approaches in the L-PBF process have been proposed and developed, such as printing with multiple lasers and optimizing process parameters for higher productivity. Other approaches like increasing the number of parts per build can decrease the print time per part, as can be a reduction in total part height (Ref 3).

The specific approach in this work is to examine the role of layer thickness, one of the key process parameters in the L-PBF process, along with power, velocity and hatch distance (Ref 4). Increasing layer thickness has a very direct effect on reducing build times since it reduces the number of slices one needs for a given part and orientation. This in turn means fewer layers for the laser to scan, as well as fewer layers for the coater blade to have to deposit fresh powder for, which are the two main components of build time in the L-PBF process. However, it has been shown that increasing the layer thickness can negatively affect properties of the manufactured parts, with reductions in density, Ultimate Tensile Strength (UTS) and

hardness documented (Ref 5). This is in part attributable to variations in the Volumetric Energy Density (VED) that is incident on the powder bed, which has been shown to influence microstructure (Ref 6, 7).

Several studies across a wide range of alloys have evaluated the effect of changing layer thickness on the properties of the resulting structures. Design of Experiment (DOE) studies using a pulsed laser on iron powder demonstrated that layer thickness is a critical variable influencing density of as-built parts; however, this was evaluated over a relatively large thickness range of 200–400 μm , with the authors concluding that the 200 μm thickness was optimum for minimizing porosity (Ref 8). A similar conclusion was obtained on a study using 18Ni-300 steel over a range of 30–60 μm , concluding that density reduced with increasing layer thickness, and that it also negatively impacted macro-hardness but had no effect on micro-hardness, with no results reported for layer thickness effects on other mechanical properties (Ref 9). Other iron-based materials were studied with a total of 20 specimens each on two different L-PBF equipment sets, one with and one without, a heated bed, at a thickness range of 20–60 μm using a DOE approach, concluding that increase in layer thickness reduced tensile strength and elongation (Ref 10). Effects of heat treatment were not studied, nor attempts to correlate behavior to microstructure. A DOE approach was also applied to studying effects of several parameters including layer thickness (20–35 μm) on Ti6Al4V, also finding reductions in density with thickness (Ref 11).

More relevant to this paper, a few recent studies have examined the role of layer thickness on L-PBF of Inconel 718 specifically. The first of these examined effect of changing layer thickness from 20–50 μm , but reported microstructure and mechanical properties only on as-built specimens without heat treatment of any kind and did not report on sample sizes used to establish mechanical properties (Ref 12). In addition to these publications, several authors have conducted studies on L-PBF of Inconel 718 with a wide range of process parameters, compiled in Table 1. Most choices of layer thickness values lie in the 20–50 μm range, with only two references exceeding 50 μm .

To a first approximation, the total print time in an L-PBF process can be said to be composed of scanning time (the time it takes to melt each layer with the laser) and the coating time (the time it takes for the coater blade to deposit a layer of powder and for the scanning to begin). Simplifying this approach by assuming a rectangular prism of a certain length, width and height being melted, and neglecting nuances of scan strategies, we can estimate these two time terms as:

$$\text{Scanning time} = \frac{\text{length}}{\text{scan velocity}} * \frac{\text{width}}{\text{hatch distance}} * \frac{\text{height}}{\text{layer thickness}} \quad (\text{Eq 1})$$

$$\text{Coating time} = \frac{\text{height}}{\text{layer thickness}} * \text{time for one coat} \quad (\text{Eq 2})$$

Adding these two times gives us the total time for printing a rectangular prism. For a velocity of 1400 mm/s and a hatch distance of 0.08mm, and a coating time of 7.5 s, the relationship of total time to print ten 10mm cubes as a function of layer thickness can be plotted and is shown in Fig. 1. This demonstrates that increasing layer thicknesses can have a significant impact on the total print time, especially when starting from low layer thickness values. Beyond a certain point however, increasing layer thickness does not provide proportional benefits to print time reduction. This is true for the geometry under consideration in this example, which does not occupy a significant portion of the build volume. As total build volume increases, laser scan velocity is expected to be a more significant role in overall print time.

This work first establishes optimum processes at each of three different layer thickness values: 30, 60 and 80 μm , prior to establishing the effects of these thicknesses on structure and properties. This work differs from prior studies in two ways: first, in its approach of separating the process optimization at each layer thickness, from the study of relating layer thickness to mechanical properties. In so doing, this work places emphasis on developing a methodology for increasing layer thickness in an industrial setting. Secondly, this study provides

Table 1. Process parameters in literature developed for L-PBF of Inconel 718, arranged in order of increasing layer thickness

References	Equipment	Power, W	Velocity, mm/s	Hatch distance, mm	Layer thickness, mm
Caiazzo et al. 2017 (Ref 27)	EOSINT M270	195	1200	0.09	0.02
Wang et al., 2012 (Ref 28)	Self-developed	170	417	NA	0.02
Sochalski-K. et al., 2015 (Ref 29)	NA	185	1200	0.1	0.02
Choi et al., 2017 (Ref 30)	Concept Laser MLab	90	800	0.08	0.025
Xia et al. 2016 (Ref 31)	SLM-150 Guangzhou	110	400	0.06	0.03
Tillmann et al., 2017 (Ref 32)	SLM250HL	175	620	0.12	0.03
Alafaghani et al., 2018 (Ref 33)	EOSINT M 280	400	NA	NA	0.04
Kelley, 2016 (Ref 34)	EOSINT M 280	285	960	0.1	0.04
Popovich et al. 2017 (Ref 35)	SLM 280HL	250	700	0.12	0.05
Sufiarov et al. 2014 (Ref 36)	SLM 280HL	245	755	0.09	0.05
Amato et al., 2012 (Ref 37)	EOS M270	200	1200	NA	0.05
Jia and Gu, 2014 (Ref 38)	NA	130	400	0.05	0.05
Nguyen et al., 2018 (Ref 12)	3D Sys. ProX-300	285	2500	0.05	0.02–0.05
Sadowski et al., 2016 (Ref 39)	EOSINT M 280	285	960	NA	0.075
Karimi et al., 2018 (Ref 40)	Renishaw AM 250	200	NA	0.1	0.075
Kuo et al., 2017 (Ref 41)	EOSINT M280	400	7000	NA	NA
Jia and Gu, 2014 (Ref 42)	NA	130	400	NA	NA

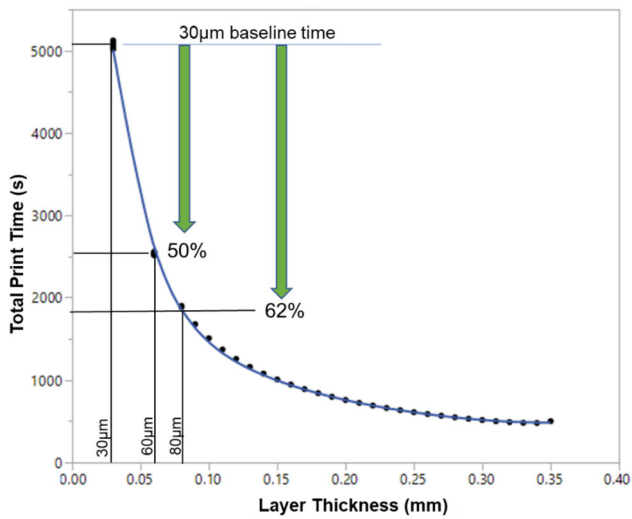


Fig. 1. Predictions made by a simple time model for print time showing relationship of time to layer thickness, and percentage reductions specific to the two layer thicknesses in this study relative to the 30 μm baseline

data from the largest sample size published yet (100 per condition), included as supplementary material. This large dataset enables a robust analysis of statistically significant differences between these layer thicknesses and correlations between surface roughness, density and mechanical properties of modulus, strength (yield and UTS) and elongation. Further, this is done for both as-printed (without specimen machining or heat treatment) and heat-treated parts to assess what improvements, if any, the heat treatment can provide to mitigate the negative effects of increasing layer thickness. Comparisons are also made to machined specimens obtained from a subsequent build on the same equipment as well as properties published for forged Inconel 718. The objective of this work is twofold: to assess if it is feasible to develop working processes at thicknesses as high as 80 μm for IN 718 on the L-PBF process and secondly to compare properties across this thickness range and develop insights into any observed differences. While the focus of the work is limited to L-PBF of this one alloy, the findings are expected to be more generally applicable.

2. Methods

2.1 Process Selection

An optimal process was first developed independently for the 30, 60 and 80 μm layer thickness values. This was done in a two-step approach: the first step involved a cliff-finding study, wherein a range of power, velocity and hatch spacing parameters were explored with 10 mm cubes to identify those that yielded specimens with sufficiently good print quality, as determined visually. This information was used in the second step to define the upper and lower bounds for each of these three parameters, which along with a mid-point, was used to define a full factorial 3×3 Design of Experiments (DOE), one for each layer thickness setting, as shown in Table 2. A single contour and a continuous hatching strategy were employed, with a 90 degree offset between layers.

Table 2. Process DOE parameter and values for 30, 60 and 80 μm thicknesses

	Low	Medium	High
<i>Layer thickness: 30 μm</i>			
Power (W)	100	200	300
Velocity (mm/s)	300	800	1300
Hatch spacing (mm)	0.09	0.115	0.14
<i>Layer thickness: 60 μm</i>			
Power (W)	150	250	350
Velocity (mm/s)	220	720	1220
Hatch spacing (mm)	0.07	0.09	0.11
<i>Layer thickness: 80 μm</i>			
Power (W)	150	220	290
Velocity (mm/s)	350	725	1100
Hatch spacing (mm)	0.08	0.09	0.10

A total of 108 10 mm cubes were printed, 27 in each of four quadrants of a Concept Laser M2 400W single-laser powder bed fusion system, as shown in Fig. 2, yielding four replicates per DOE condition. The variation in the colors of the tops of the cubes is on account of the varying surface textures obtained at different combinations of parameters in Table 2. All 108 cubes for each of the three layer thicknesses were removed from the build plate using wire Electrical Discharge Machining (EDM) without any heat treatment. Density was calculated using the Archimedes method (Ref 13, 14), with each cube measured three times and an average obtained. Obtained values were converted to a relative density value comparing it to a baseline density for Inconel 718 derived from averaging different values obtained in industry datasheets as 8.196 g/cm^3 (Ref 15, 16). Plots of relative density versus Volumetric Energy Density (VED) were created and are shown in Fig. 3, with VED computed using the formulation (Ref 17):

$$\text{Volumetric Energy Density} = \frac{\text{Power}}{\text{Velocity} * \text{Hatch Distance} * \text{Layer Thickness}} \quad (\text{Eq 3})$$

VED, while a useful metric, does have challenges when used as the sole process selection metric (Ref 17). However, the data in the graphs on the left in Fig. 3 for each of the three thicknesses show an increase in relative density with increasing VED up to a certain threshold, after which the relative density saturates close to the maximum value, and beyond a second threshold starts to drop again. These data corresponded well to observations of lack of fusion at low VED values and over-sintering at high VEDs. As a result, upper and lower VED thresholds were established for each of the three thicknesses, as shown with the dotted lines on the left graphs in Fig. 3. To select a process for this study, relative density values across the four quadrants were averaged and the average values within the VED thresholds were re-plotted—the VED thresholds thus bounded a working process window with as-printed relative densities in excess of 98.5%. A specific VED that yielded a result right in the middle of this window was selected on the basis of the argument that this process would in principle have the widest process margin and better tolerate variations in local heat conduction resulting from variations in geometry. This approach was thus used to select a process at each of the three layer thicknesses in this study, with finalized parameter sets

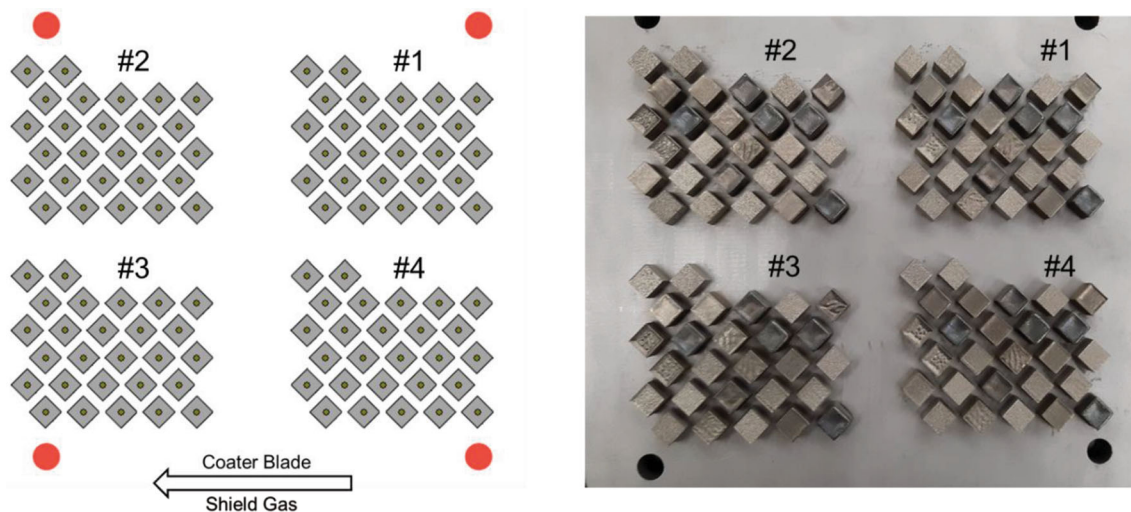


Fig. 2. Build preparation setup and final build for each of the three layer thicknesses evaluated in this study, showing four replicates of a 27 cube DOE. Each cube has a 10mm side

provided in Table 3. All specimens involved in subsequent discussion were fabricated with these parameters.

Cubes with the selected process parameters for each of the three thicknesses were sectioned, polished, etched and imaged per established methods for Inconel 718 (Ref 18). The objective of obtaining these metallographic images was to qualitatively verify the density values being obtained and also ensure the melt pools conformed to expectation. Figure 4 indeed shows evidence of both these points, with micrographs along the build direction demonstrating negligible porosity and melt pools corresponding to the different layer thicknesses, showing adequate inter-layer melting even for the 80 μm layer thickness.

2.2 Specimen Design and Manufacturing

A tensile test specimen geometry was selected based on the ASTM E8 standard (Ref 19). In this study, a plate type specimen was selected and designed as shown in Fig. 5(a), with 2 mm selected for the thickness. Finite Element Analysis was conducted on this specimen design to ensure stress concentration factors was under 1.1, which was obtained for a corner radius of 18 mm between gauge and grip sections of the specimen. All specimens were manufactured in the vertical orientation only, as shown in Fig. 5(b). A single contour scan strategy was employed with a 90 degree hatching offset from one layer to the next, matched to the scan strategy used in the previous study with 10 mm cubes. Laser parameters specified in Table 3 were used for the three different layer thicknesses. Since the primary goal of this study is to assess the feasibility of increasing layer thickness in the powder bed fusion of Inconel 718 and assess its effects on mechanical properties, the vertical orientation is expected to enable a direct assessment of this since the loading direction experienced by the specimens is along the build direction. A 10 \times 10 matrix of specimens was successfully built as shown in Fig. 5(b)—one build of 100 specimens was manufactured at 30, 60 and 80 μm layer thickness each. A second set of three such builds was then fabricated again. All six builds were fabricated on the same Concept Laser M2 400 W single laser machine, with Argon

used as the inert gas. Powder used in all these builds had been recycled at least three and no more than ten times. Specimens in the first three builds were removed from the build plate using the wire EDM process right after printing, with no heat treatment (“as-printed”). Builds 4 through 6 went through standard stress relief preceding specimen removal, followed by Hot Isostatic Pressing (HIP) and final aging and solutionizing heat treatments, following recommendations in ASTM F3055-14a and AMS2774E. The stress relief step had an initial ramp to 1400°F for 2 h, followed by a ramp to 1950°F for 90 min. An examination of the thermal profiles after heat treatment showed that the specimens also went through an additional, unintentional solutionizing step at 1750°F for 1 h due to a programming error, though this was assessed to be of low impact due to the higher temperatures in the subsequent HIP step. HIP was conducted at 100 MPa and 2048°F for four hours. Final heat treatment consisted of a solution set temperature of 1750°F for 1 hour, followed by a precipitation set temperature of 1325°F for 8 hours with a cooling rate as specified in AMS 2774E.

In summary, a total of 600 specimens were manufactured across six builds, 200 at each of the three build layers. Half of these were characterized and tested in an as-printed state, the other half received heat treatment prior to data collection. As a result, all subsequent data are presented with these two distinguishing variables: layer thickness (30, 60 or 80 μm) and post-processing (as-printed or heat-treated).

2.3 Characterization and Testing

2.3.1 Surface Roughness.

Prior to mechanical testing, specimens were scanned using a Keyence VR-3200 scanning microscope which uses structured white light (Ref 20). A 5 mm diameter circle was scanned on the flat section of the specimen, 5 mm from the top edge (in the build direction). An area average, S_a , was computed from each scan based on a calculated reference plane, conducted at the high magnification setting with 40 \times zoom. S_a provides mean surface roughness by

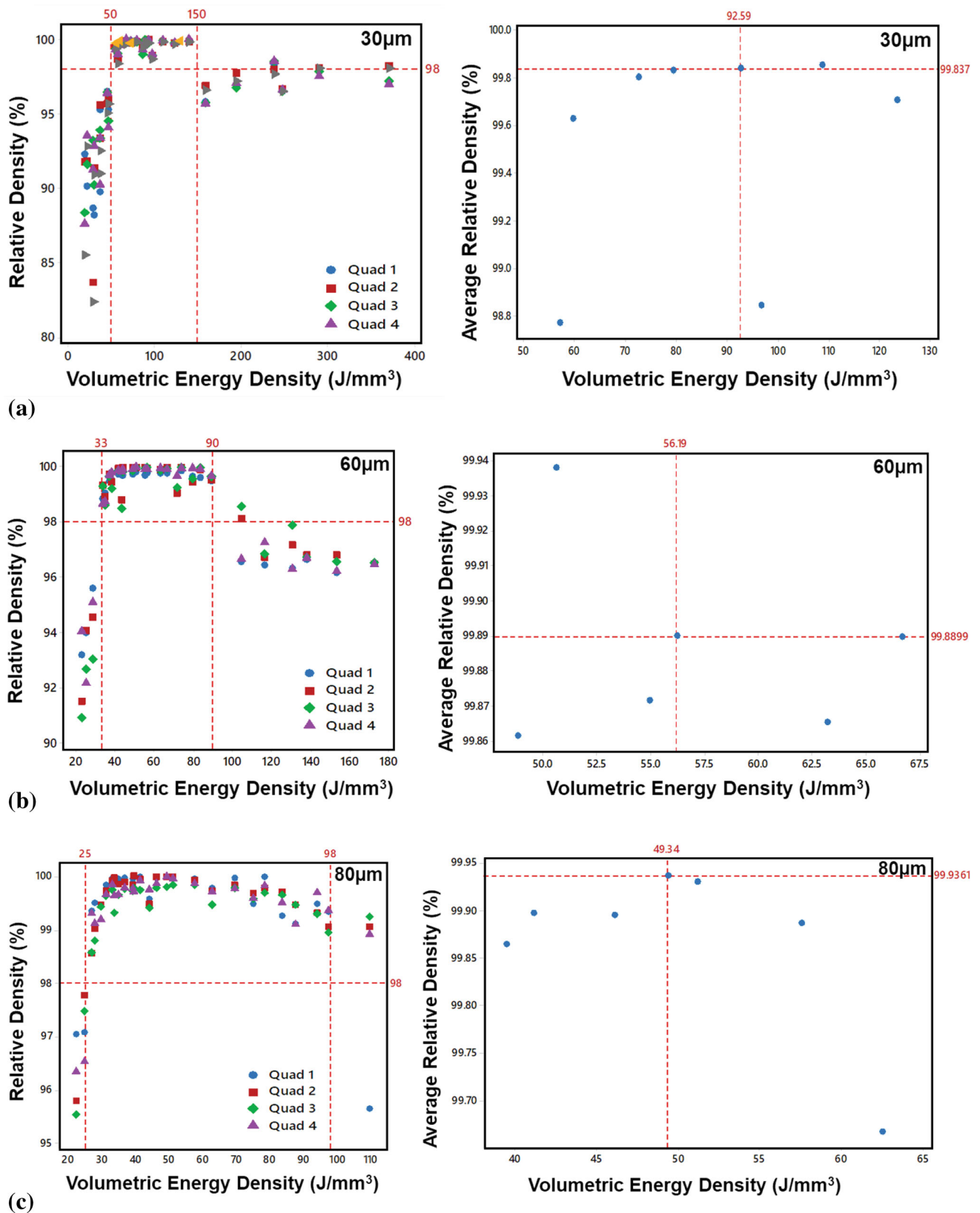


Fig. 3. Relative density (Archimedes method) plotted as a function of Volumetric Energy Density (VED) for (a) 30, (b) 60 and (c) 80 μm layer thicknesses. Graphs on the left show results for all 81 cubes, color coded by quadrant. Graphs on the right show how the process was selected based on being in the mid-range of the high relative density values for each thickness to maximize process margins

Table 3. Selected process parameters for each of three layer thicknesses in this study

Layer Thickness, μm	Power, W	Scan velocity, mm/s	Hatch spacing, mm	VED, J/mm^3
30	200	800	0.09	92.59
60	220	725	0.09	56.19
80	300	950	0.08	49.34

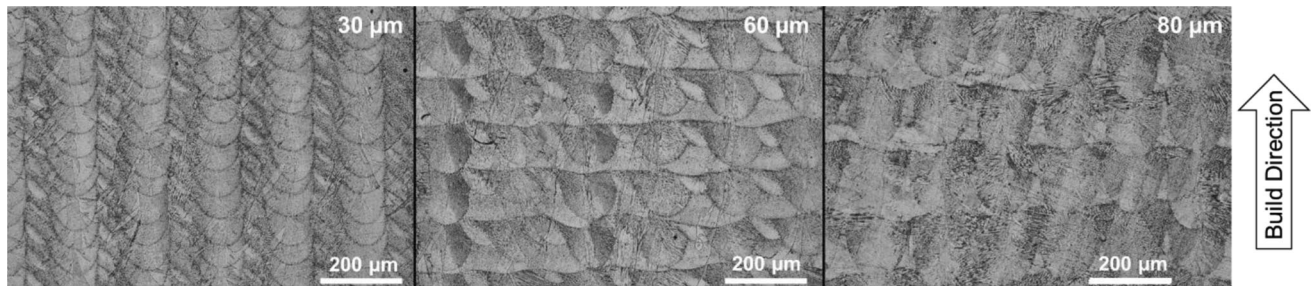


Fig. 4. Micrographs for the three different layer thicknesses in this study, showing negligible porosity and clear melt pool formation in correspondence to layer thickness, for as-printed cube specimens

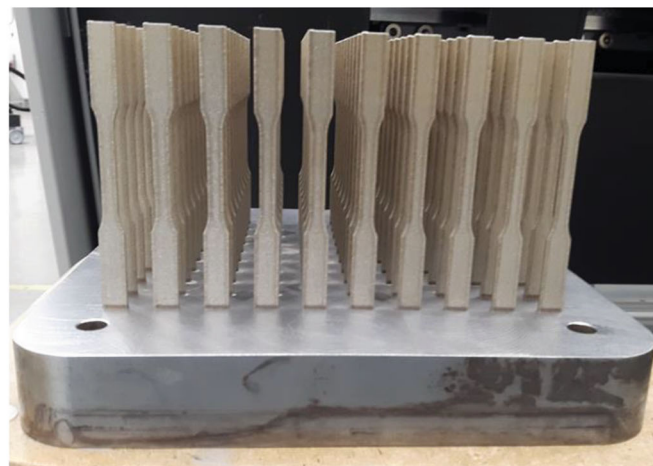
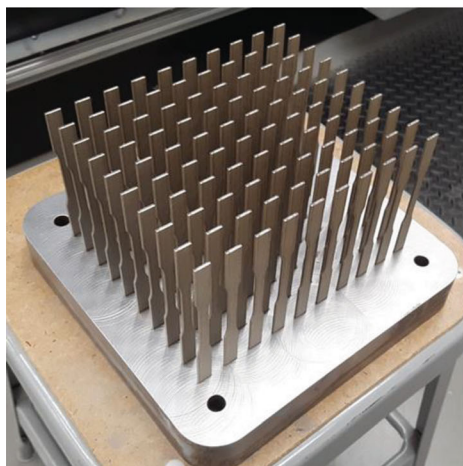
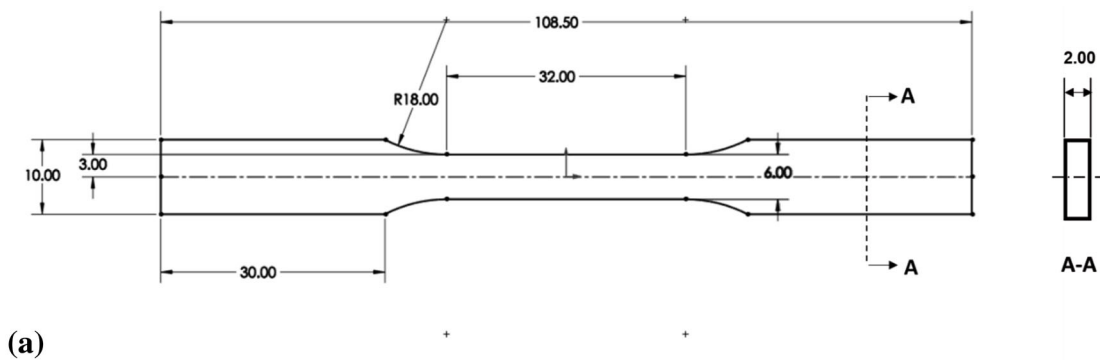


Fig. 5. (a) Rectangular section specimen design developed for this study and (b) array of 100 tensile test specimens, all printed in the vertical orientation. Six such builds were fabricated for this study, two at each of the three different layer thicknesses

calculating the difference of the height of a peak and valleys from the arithmetical mean plane of the surface, computed as a reference plane in the software. In-built reference plane

correction was applied to correct for any specimen warpage. Surface roughness was measured for all 600 specimens in this study. The purpose of collecting surface roughness data is

twofold: to examine the hypothesis that increasing layer thickness increases surface roughness and to examine correlations to mechanical property data.

2.3.2 Archimedes Method. The Archimedes method was selected due to its ease of use and relative accuracy at high density values (Ref 14). In addition to the more typical use of the method for estimating density of additively manufactured cubes, Archimedes density was also estimated in this study for all 600 dog-bone specimens, prior to mechanical testing. A specially designed density measurement kit with an analytical balance with 0.0001 g precision was used with distilled water as the liquid for immersion.

2.3.3 Mechanical Testing. Tensile tests were conducted on all 600 specimens following guidelines documented in ASTM E8, using a tensile strain rate of 10^{-3} s^{-1} (displacement rate of 1.5 mm/min over a nominal gauge length of 25 mm) and tested on an INSTRON 5985 (Ref 21). Specimen cross-section thickness was measured using a standard micrometer and width using calipers to obtain a section area, which was used for computation of stress. Strain was reported using an in-built non-contact video extensometer. Raw data from the machine were extracted to a MATLAB code, a representative set of which is shown in Fig. 6. ASTM E8 guidelines were then used to further estimate elastic modulus, yield strength, engineering Ultimate Tensile Strength (UTS) and percent elongation using the automated code with manual verification to ensure no spurious results.

2.3.4 Microstructure. Untested specimens were sectioned within the gauge, polished to $0.05 \mu\text{m}$, etched with Kalling's reagent and imaged using a FEI Nova 200 SEM.

3. Results

For the 100 specimens built with the parameters in Table 2, the actual build times for the 30, 60 and $80 \mu\text{m}$ layer thickness builds amounted to approximately 46.5, 24.5 and 17.5 h, respectively. The higher 60 and $80 \mu\text{m}$ layer thicknesses thus represented a 48% and 63% reduction respectively, relative to the $30 \mu\text{m}$ build time, which is a substantial improvement in

build rate. These numbers also agree well with the simple model proposed earlier (Fig. 1), which predicted a 50% reduction when moving from a 30 to $60 \mu\text{m}$ layer thickness and a 62% reduction when moving from 30 to $80 \mu\text{m}$ layer thickness. The benefits of increasing layer thickness on productivity are thus evident. This section examines how the increase in layer thickness impacted properties.

3.1 Surface Roughness

Surface roughness S_a values obtained from this study are shown in Fig. 7(a) and (b), for each of the three layer thicknesses and for both post-processing conditions. It is clear that surface roughness increases as layer thickness increases—this trend is maintained both in the as-printed specimens as well as the heat-treated specimens. A height map scan with a Keyence 3D scanning microscope (Fig. 8a) shows how the presence of the layers becomes increasingly evident as the layer thickness increases. This is also visible in the SEM images shown in Fig. 8(b) and (c), the latter at higher magnification. The layering of melt pools is most evident on the edges, with the feature becoming more prominent as layer thickness increases. While the laser parameters (power, velocity and hatch spacing) at each layer thickness vary, the profile shows that layer thickness is the dominant factor driving the differences in surface morphology. These height map and SEM images validate the hypothesis that surface roughness increases with increase in layer thickness, with statistically significant differences observed from $30 \mu\text{m}$ to the larger thicknesses.

3.2 Archimedes Density

Obtained density values from all 600 specimens are plotted in Fig. 9(a) and (b), for as-built and heat-treated specimens, respectively. The HIP process within the heat treatment steps clearly increased density for each of the three layer thicknesses, but also increased the standard deviations associated with these measurements. The as-printed density values do not show a trend in relation to layer thickness, but a trend emerges after HIP and heat treatment, with mean density reducing with

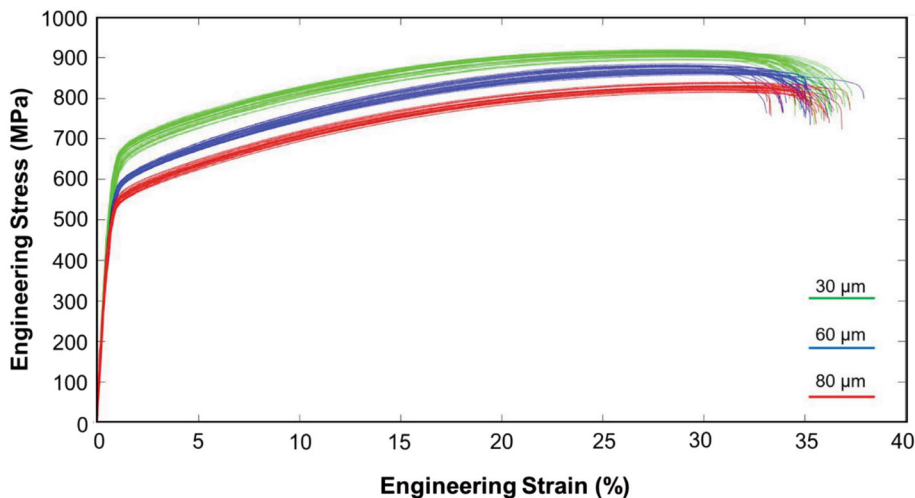


Fig. 6. Representative stress-strain curves obtained in this study for each of the three layer thickness specimens (30 specimens per condition shown here, in the as-built condition)

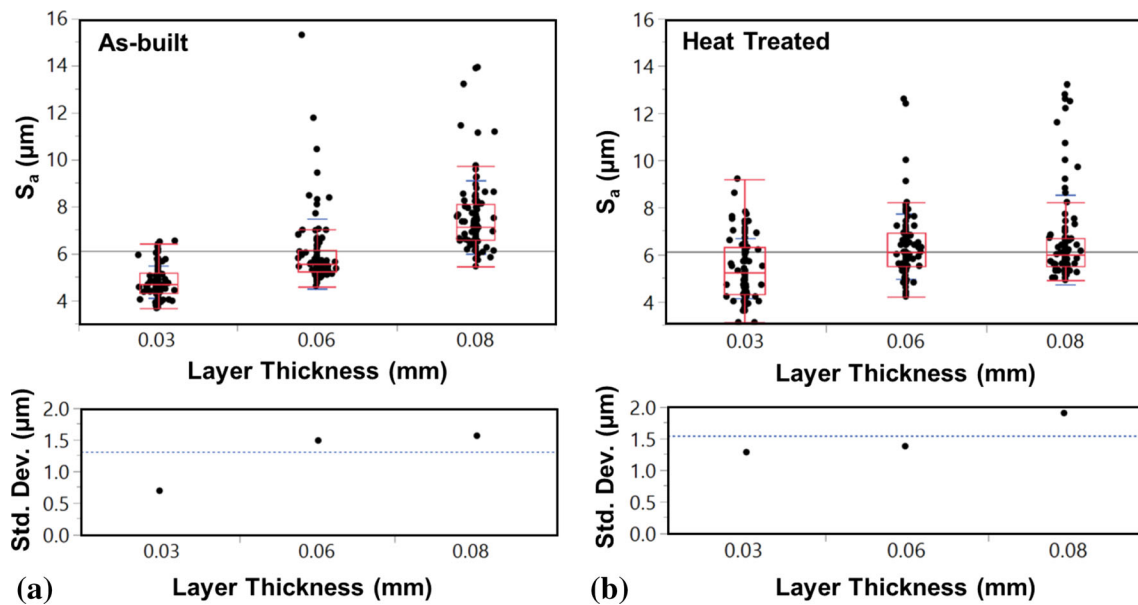


Fig. 7. Surface roughness (S_a) data for all three layer thicknesses (a) as-built and (b) after heat treatment. Horizontal lines represent mean values across all layer thicknesses for that build condition

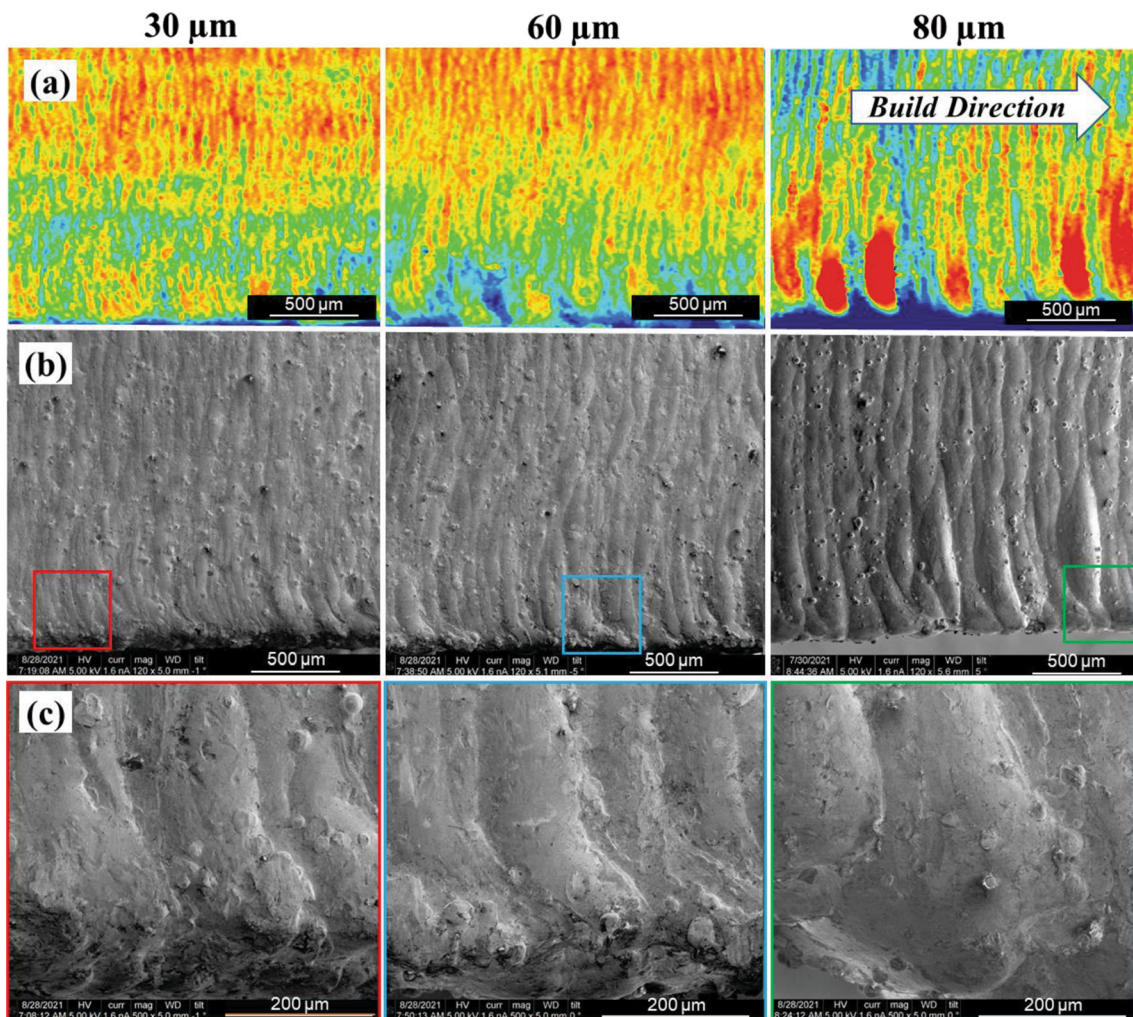


Fig. 8. Comparison of surface texture for the 30, 60 and 80 μm layer thicknesses after heat treatment, all taken at the edge of the specimen: (a) height map generated from a scanning microscope, (b) and (c) SEM images at two different magnifications (see scale bar)

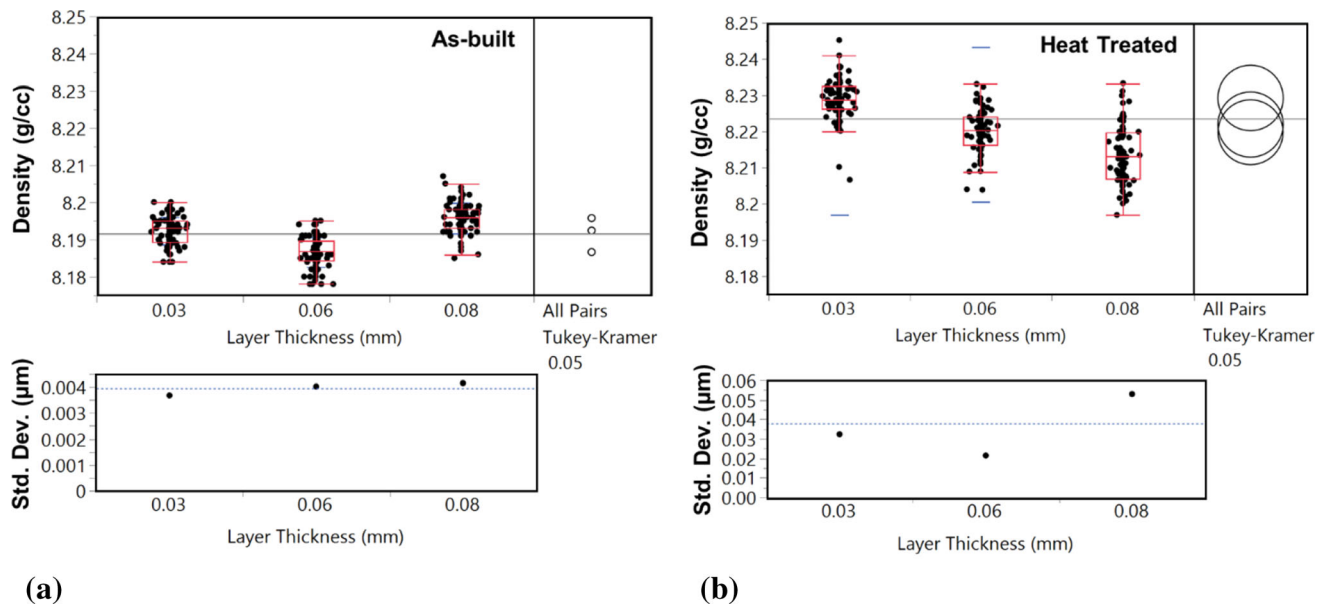


Fig. 9. Archimedes density data for all three layer thicknesses: (a) as-built and (b) after heat treatment

increase in layer thickness while standard deviations associated with them increases.

3.3 Mechanical Properties

A selection of stress–strain graphs obtained from mechanical testing is shown in Fig. 6, for three layer thickness conditions in the as-built condition and show a fairly well behaved response in line with expectations. These data were used to extract four of the most important metrics which are plotted in Fig. 10(a), (b), (c) and (d), with comparisons to AMS 5663 published values for forged Inconel 718 included for each. It is to be noted that forged properties are A-basis design values, whereas the obtained results in this paper derive from the specific study conducted here. Heat treatment (including HIP) has the expected effect of increasing modulus and strength while decreasing elongation. Yield strength and UTS show reduction with increase in layer thickness, a fact that is evident even after heat treatment. Modulus does not show significant dependence on layer thickness. Elongation shows no dependence in an as-printed state, but differences are evident after heat treatment. Post-heat treatment values for strengths are comparable to forged Inconel 718 with significantly higher elongation and lower modulus observed. Of importance to note is that these are all specimens that received no mechanical finishing or machining after manufacturing and thus retain their post-print surface morphologies at the time of testing.

3.4 Microstructure

SEM images were taken for untested, heat-treated specimens, from sections made that revealed the X-Y (viewed along the build direction) and X-Z (viewed perpendicular to the build direction) planes, shown in Fig. 11(a) and (b), respectively. For each layer thickness and plane, SEM images were obtained at three different zoom levels. Prior literature of microstructural studies in L-PBF generated Inconel 718 (Ref 22–26) were consulted in an effort to identify phases and compare against. The collection of SEM images in Fig. 11(a) and (b) shows no significant difference in microstructure across the three layer

thicknesses for both planes. As expected, melt pool boundaries seen in the as-built condition (Fig. 4), can no longer be seen in the heat-treated parts.

For the X-Y plane images in Fig. 11(a), the amount of laves phase in the final heat-treated parts is diminished when compared to the as-built condition (Ref 22, 23, 25). The large precipitates (delta phase and carbides) can primarily be seen along the grain boundaries, consistent with prior research (Ref 26). Annealing twins can be found for all three layer thicknesses, and the twin boundaries are devoid of precipitates. Grain sizes and distributions are relatively unchanged across the 3 different layer thicknesses. A variety of grain sizes can be seen ranging from 100 microns across to 10 microns (not including the annealing twins).

For the X-Z plane images in Fig. 11(b), the grains demonstrate some of the tall aspect ratio expected from the directional diffusion of heat from the L-PBF process. Grain annealing can be found, but it is evident that the carbides inhibit grain growth. Annealing twins can be found for all 3 layer thicknesses, similar to those visible in the XY plane. It appears that the number of carbides and delta phase precipitates increases slightly with increasing layer thickness, but delta phase sizes are relatively consistent. Grain sizes and distributions are relatively unchanged across the 3 different layer thicknesses. Given these similarities, one can conclude that, with the exception of a slight increase in precipitates with layer thickness, a similar microstructure was obtained for all three layer thicknesses and their respective processes in this work.

4. Discussion

This work was motivated by a need to assess the feasibility of developing a manufacturable process at increasing layer thicknesses and additionally assess the debits associated with it. Of most interest is the mechanical behavior after industry-standard stress relief, HIP and heat treatment, which showed that while elastic modulus of all three layer thicknesses were

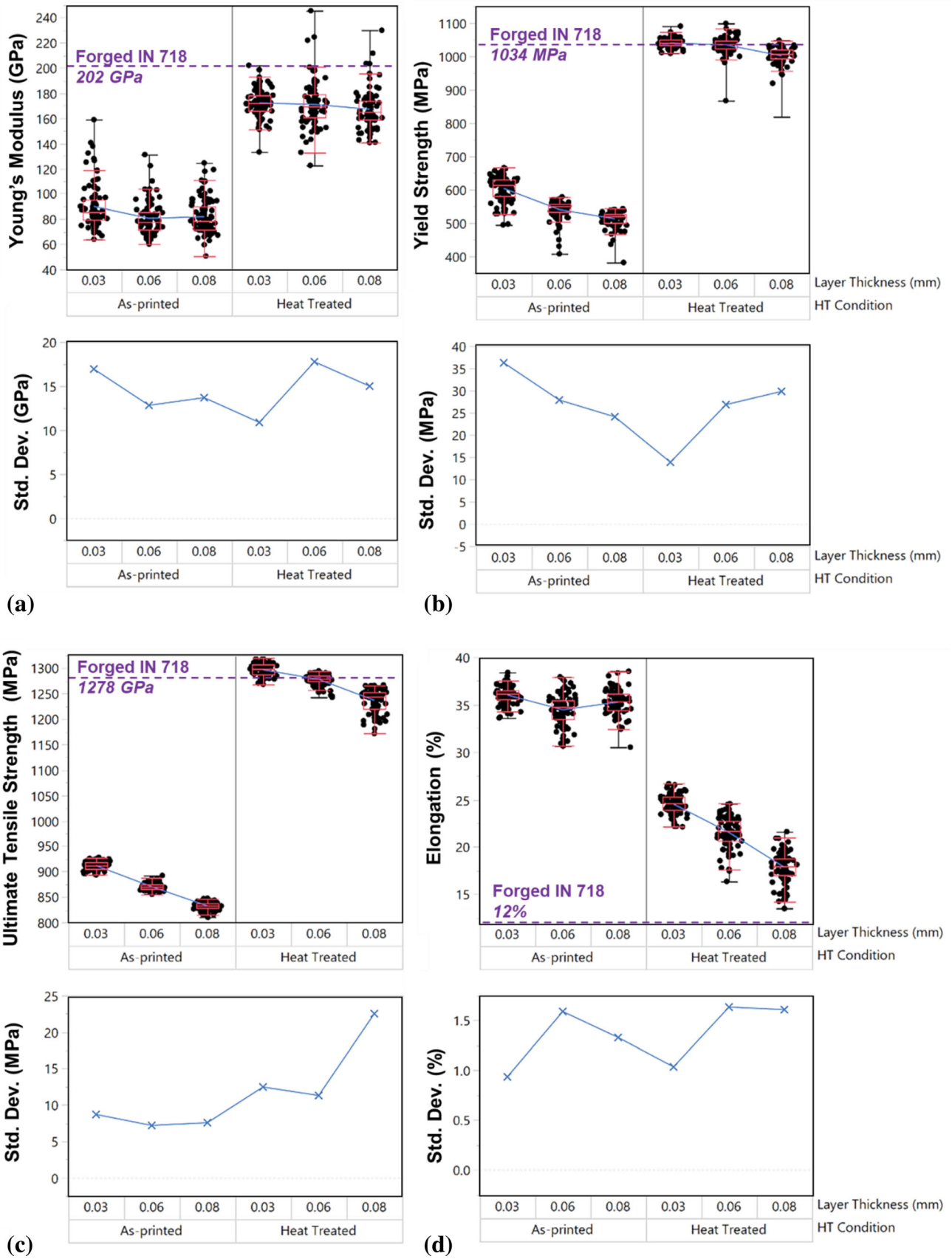


Fig. 10. (a) Elastic modulus, (b) yield strength, (c) Ultimate Tensile Strength and (d) percent elongation (right), as a function of heat treatment condition and process build layer thickness

fairly similar, a statistically significant drop was noticed in yield strength, UTS and elongation as layer thickness increased. The total reduction on the mean values for both strengths from 30 to 80 μm layer thickness is 3.7% for yield and 4.6% for UTS, with the 60 μm layer results in between. In this section, these results are placed in context by providing comparisons to forged and machined properties, performing correlation studies and examining variances. While these discussions are based on data collected on the Concept Laser M2 system, the underlying arguments are expected to be valid for other L-PBF systems as well, with some variation in the mean values of material properties to be expected.

4.1 Comparison to Forged and Machined Data

One way of contextualizing the above datasets is to compare the mean values obtained for each of the three layer thicknesses against data available for forged Inconel 718. Another way to assess this is to evaluate it against specimens that were

machined, instead of tested in their as-printed morphology, but using the same process parameters and equipment used to fabricate the specimens in this study. A parallel study of high temperature behavior of the higher thickness layers was conducted by an industry partner. Fourteen specimens were fabricated using the same process parameters developed for the 60 and 80 μm layer thicknesses each—30 μm layer thickness was not studied since the partner company already had sufficient internal data at this thickness. Instead of the plate-like specimens used before, 0.5 inch (12.7 mm) cylinders were manufactured which were then machined down to a 0.25 inch (6.35 mm) gauge diameter with a 1 inch (25.4 mm) gauge length and tested under uniaxial tension at a strain rate of $5 \times 10^{-3} \text{ s}^{-1}$ at seven different temperatures from room to 1600 F (871 C), following ASTM standards E8 and E21. This strain rate was chosen by the industry partner in keeping with internal practice—while different from the one used in this study ($1 \times 10^{-3} \text{ s}^{-1}$), it is still within the same order of

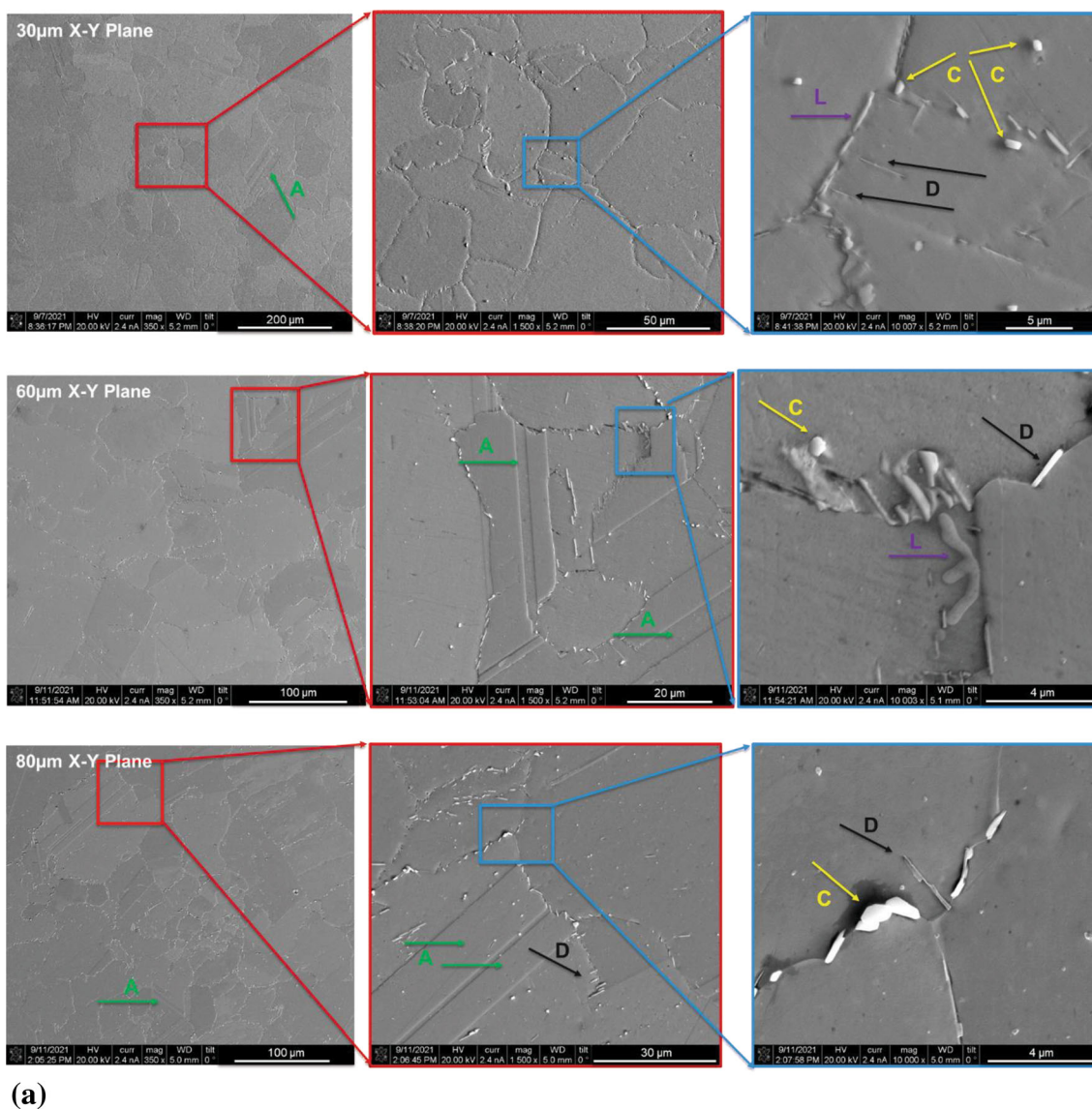


Fig. 11. Scanning electron microscopy (SEM) images showing microstructure of specimens after heat treatment for each of the three layers for (a) X-Y plane (looking along build direction) and (b) X-Z plane (looking perpendicular to build direction). Arrows indicate features of interest: A—Annealing twins, C—Carbides, D—Delta precipitates, and L—Laves phase

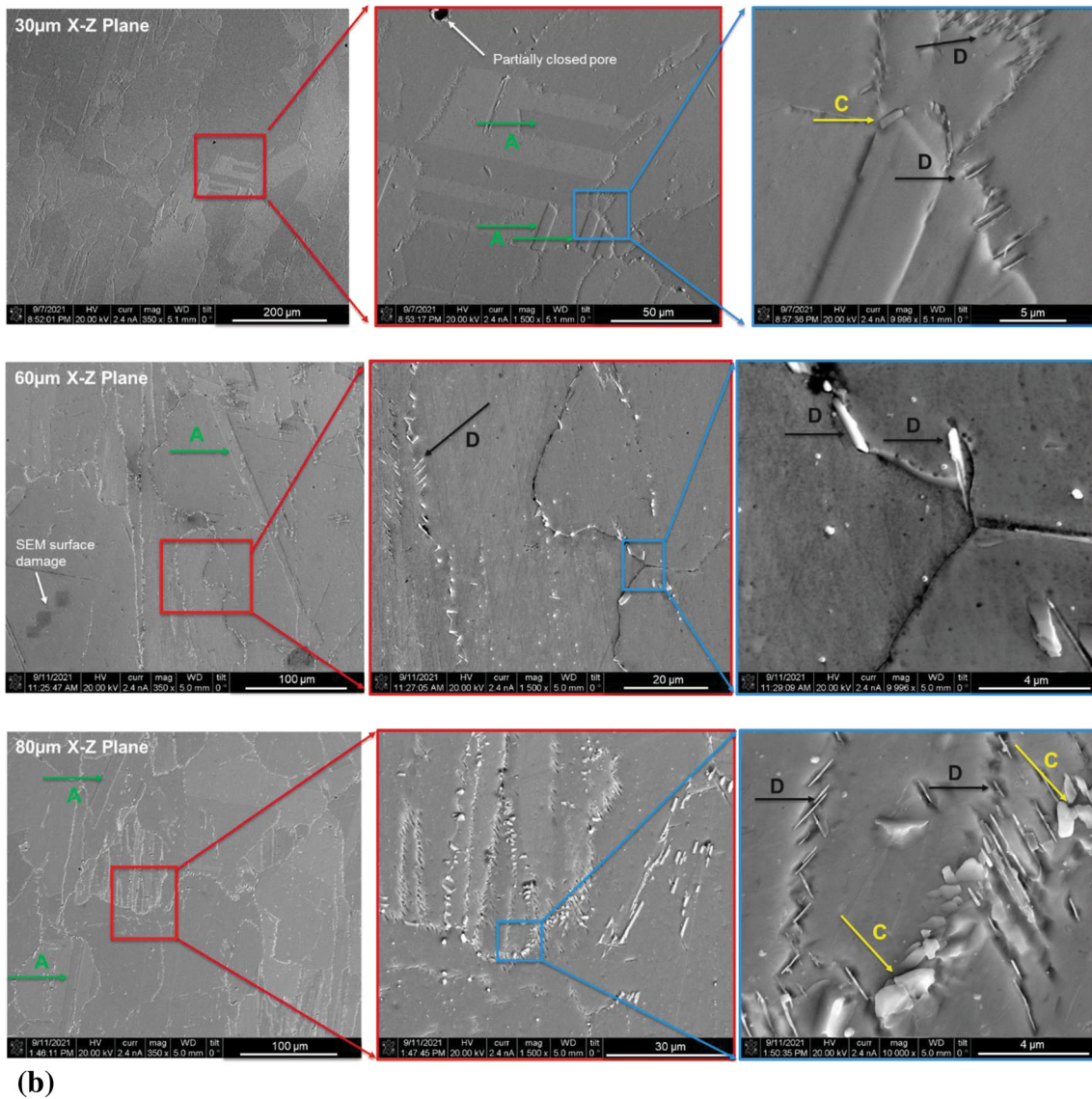


Fig. 11. continued

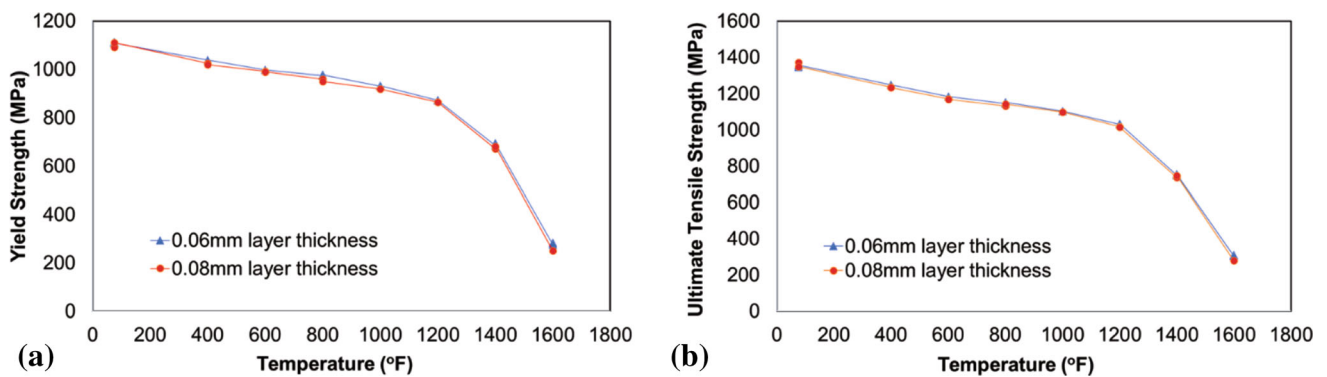


Fig. 12. Comparison of high temperature (a) yield strength and (b) Ultimate Tensile strength for machined specimens at 60 and 80 μm layer thicknesses

magnitude to permit a valid comparison. While the cylinders were additively manufactured on the same machine used in the above work, heat treatment and HIP, as well as the mechanical

testing, was carried out at the industry site, but following the same specifications used in this work. The obtained yield strength and UTS for these specimens are shown in Fig. 12 for

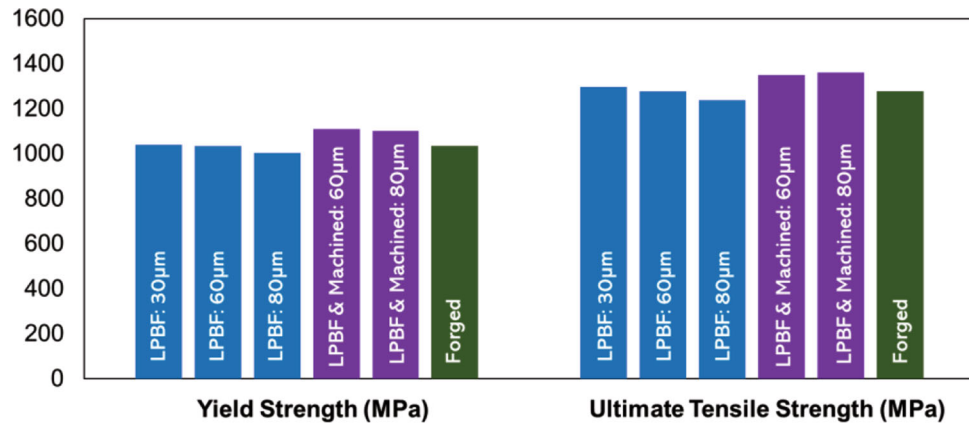


Fig. 13. Comparison of mean yield and Ultimate Tensile strengths estimated in this study for post-heat-treated L-PBF specimens against machined L-PBF specimens and specification values for forged Inconel 718

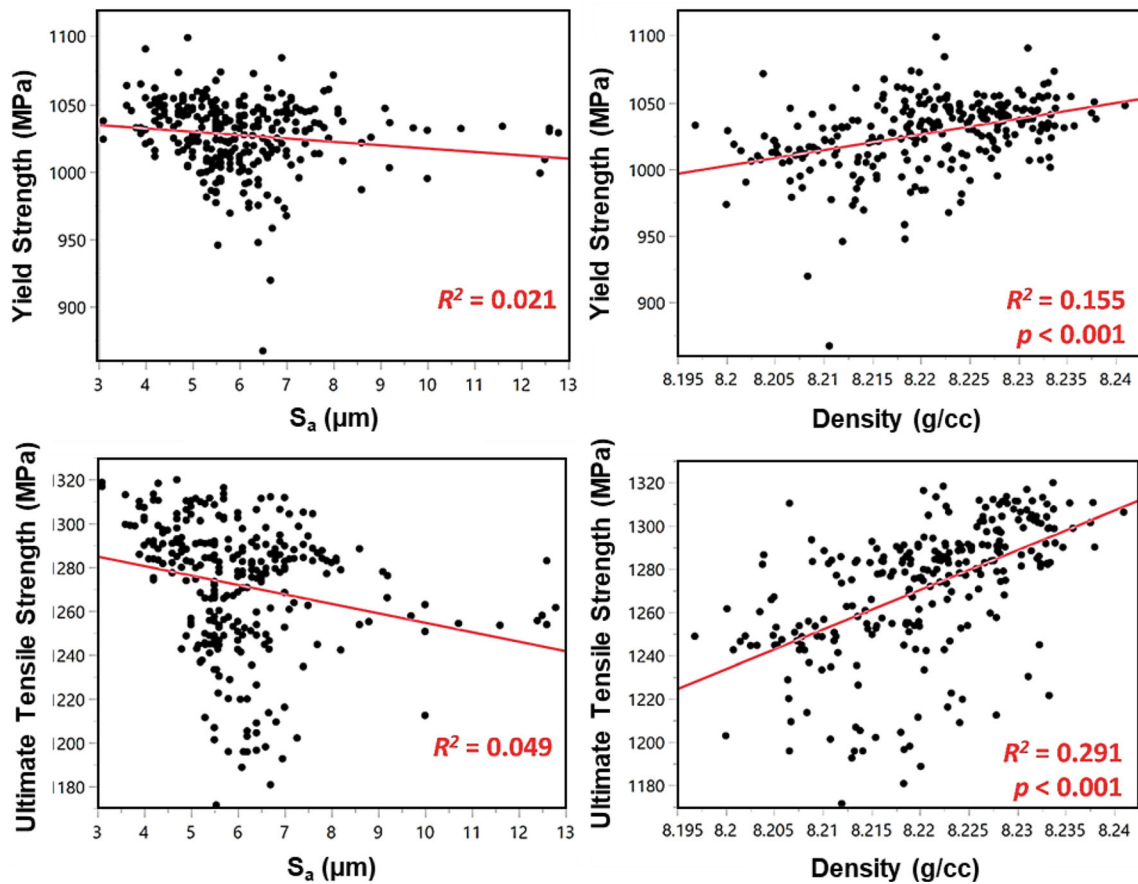


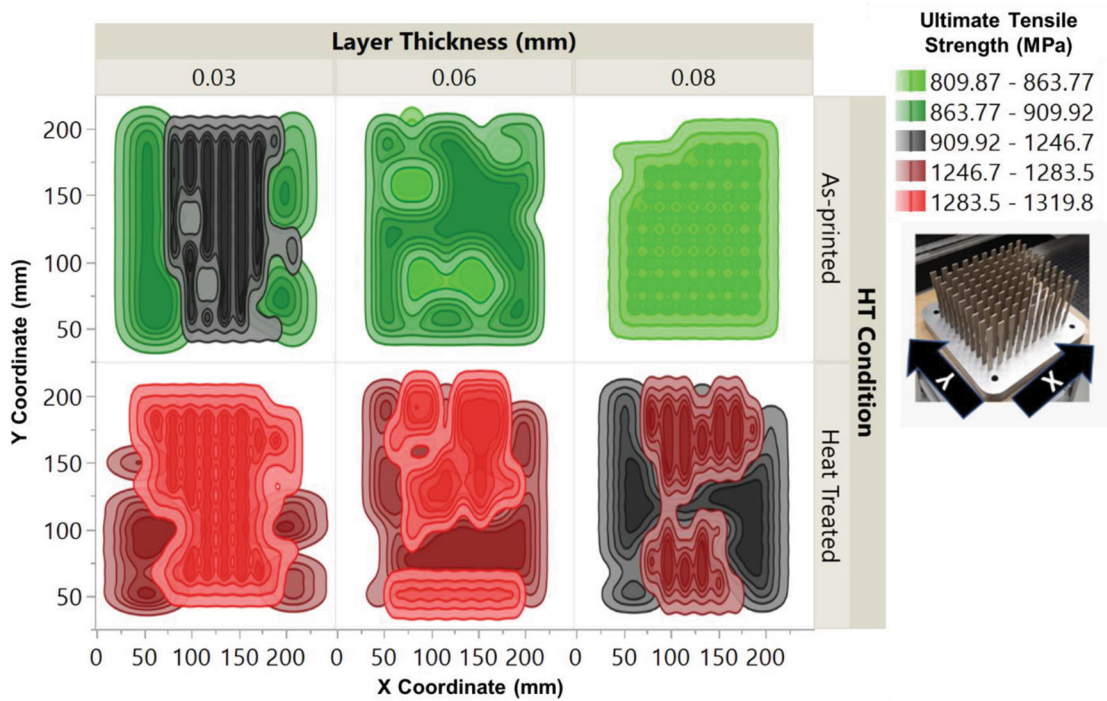
Fig. 14. Correlation plots for yield strength and UTS versus surface roughness and density. Density values above 8.25 g/cc were removed prior to analysis and are not shown here

both layer thicknesses studied, at the seven different temperatures tested, with two specimens tested for each condition. This dataset shows that machined specimens have little differences in strength between the two layer thicknesses, across the temperature range studied. The machined specimens also have higher strength than that obtained for the specimens in this study without machining and also outperform reported forged Inconel 718 data, as shown in Fig. 13. This dataset suggests that the 60 and 80 μm layer thickness processes for

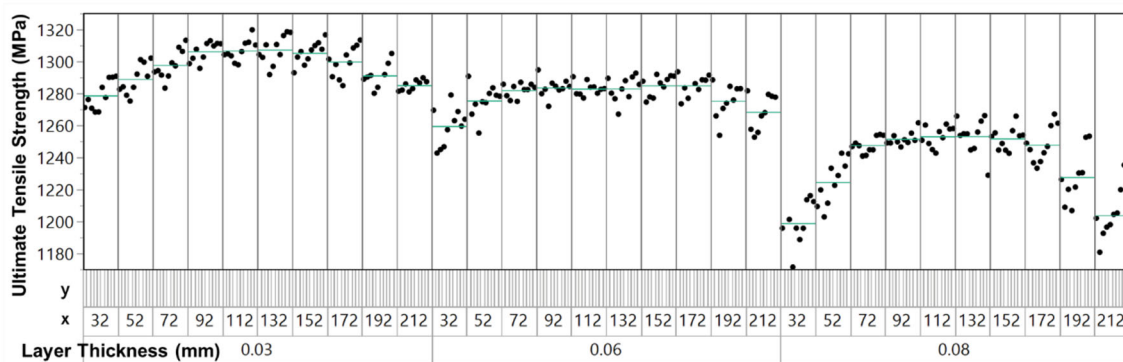
machined specimens are both robust processes. It also suggests that strength is reduced for specimens that are not machined, and further that this reduction increases with increasing layer thickness.

4.2 Correlation with Surface Roughness and Density

Characterization data for heat-treated 30, 60 and 80 μm specimens show that as layer thickness was increased, surface



(a)



(b)

Fig. 15. (a) Contour plot of Ultimate Tensile Strength for all six builds (600 specimens) for each layer thickness heat treatment condition. Green indicates lowest UTS, black is intermediate, and red is highest UTS. Inset shows X and Y direction relative to the build platform. (b) Post-heat-treated UTS across the build platform for all three layer thicknesses as a function of x and y position on the build platform

roughness increased and density reduced. It may thus be expected that one or both of these two variables may bear some correlation to the measured strength. After excluding 11 outlier density measurements in excess of 8.25 g/cc (corresponding to the upper 95% mean), the resulting data (284 data points) were plotted with linear fits to assess strength of the correlation. As shown in Fig. 14, strengths have no correlation to surface roughness, but do have weak correlation to density, with p-values for the latter below 0.001, suggesting that this relationship is a statistically significant one. Based on this data, it may be argued that the reason for the reduction in mean strength (yield and UTS) is partly attributable to the increase in porosity. The fact that this reduction is not observed for machined specimens suggests that this porosity is primarily surface-connected, and that it increases at the margins for higher layer thicknesses.

4.3 Within-Build Variation

The large dataset in this work enables a study of process variation within a build, with each build having 100 identically manufactured specimens. Since each of the 6 builds had a different layer thickness or specimen design, build-to-build variation data cannot be established. As a result, within-build data were examined to establish any trends with respect to location. None of the metrics showed a strong relationship to location, except for Ultimate Tensile Strength. As shown in Fig. 15(a), for as-printed and heat-treated specimens, across all three layer thicknesses, the highest UTS values within a build tend to occur in the middle of the build along the X-direction. In other words, the edges closest to the dose and the overflow chambers tend to have the lowest UTS. This is also evident when plotted quantitatively, as shown in Fig. 15(b), in particular for the 80 μm layer thickness specimens. No other

metric showed significant location dependence, suggesting that this behavior is uniquely attributable to UTS's dependence on stress-localizing defects such as introduced by surface morphology, for initiation of final failure in specimens when tested under tension, and further that there is a higher defect density in the L-PBF process at the edges of the build platform, and that the impact of this on UTS grows with increasing layer thicknesses.

5. Conclusions

This work examined the feasibility and resulting effects of increasing layer thickness in the laser powder bed fusion process, as specifically applied to Inconel 718 for vertically built tensile test specimens on a 400W single laser Concept Laser M2 machine. The following conclusions can be drawn from this study:

- As-printed relative densities in excess of 99% were obtained for layer thicknesses up to 80 μm
- As-printed properties show statistically significant reductions in yield strength, UTS and elongation and increases in surface roughness measured on vertical walls, with increasing layer thicknesses. No significant change in density or modulus is observed across the layer thickness range 30–80 μm .
- Stress relief, HIP and heat treatment show improvement in modulus and strength properties for all layer thicknesses, with density also showing significant reductions at higher layer thicknesses.
- Post-heat treatment UTS shows weak, but statistically significant correlation with density, and dependence with build location, especially for higher layer thicknesses.
- Post-heat treatment mechanical properties in general are comparable to forged properties. Machined specimens show significant improvement.

This work recommends a path for increasing layer thickness in the L-PBF process for Inconel 718. While there is a reduction in strength with increasing layer thickness, this reduction may be acceptable if within allowable values for the application of interest. The present study only focused on vertically manufactured specimens, and some of the findings in this study, such as surface roughness effects, could be exacerbated for 3D parts with downfacing, supported and angular, unsupported surfaces. However, this work suggests that components like functional prototypes, tooling and non-critical load bearing structures, where higher surface roughness may be tolerated, can be manufactured with the higher layer thickness process with no significant impact to part performance, and significant benefits to productivity and cost.

Acknowledgments

The team would like to thank Honeywell Aerospace Inc. for their support with problem definition, high temperature data and funding that made this work possible. Thanks are also due to Quintus Technologies, North America, for support with Hot Isostatic Pressing (HIP) and to Phoenix Heat Treating for supporting heat treatment of the 300 heat-treated specimens in

this work. Additive manufacturing, characterization and testing were all performed at Arizona State University's Manufacturing Research and Innovation Hub at the Polytechnic School in Mesa, Arizona.

References

1. D. Bhate, *Design for Additive Manufacturing: Concepts and Considerations for the Aerospace Industry*, SAE International, Warrendale, 2018
2. C. Lindemann, U. Jahnke, M. Moi, and R. Koch, *Analyzing Product Lifecycle Costs for a Better Understanding of Cost Drivers in Additive Manufacturing*, 2012
3. L. Rickenbacher, A. Spierings and K. Wegener, An Integrated Cost-Model for Selective Laser Melting (SLM), *Rapid Prototyp. J.*, 2013 <https://doi.org/10.1108/13552541311312201>
4. L. Yang, K. Hsu, B. Baughman, D. Godfrey, M. Medina, F. Menon and S. Wiener, *Additive Manufacturing of Metals: The Technology, Materials, Design and Production*, 1st ed. Springer, Berlin, 2017
5. C.U. Brown et al., The Effects of Laser Powder Bed Fusion Process Parameters on Material Hardness and Density for Nickel Alloy 625, *NIST Adv. Manuf. Ser.*, 2018 <https://doi.org/10.6028/NIST.AMS.100-19>
6. J.P. Oliveira, A. LaLonde and J. Ma, Processing Parameters in Laser Powder Bed Fusion Metal Additive Manufacturing, *Mater. Des.*, 2020 <https://doi.org/10.1016/j.matdes.2020.108762>
7. J.P. Oliveira, T.G. Santos and R.M. Miranda, Progress in Materials Science Revisiting Fundamental Welding Concepts to Improve Additive Manufacturing: From Theory to Practice, *Prog. Mater. Sci.*, 2020, **107**(2018), p 100590. <https://doi.org/10.1016/j.pmatsci.2019.100590>
8. S. Dingal, T.R. Pradhan, J.K.S. Sundar, A.R. Choudhury and S.K. Roy, The Application of Taguchi's Method in the Experimental Investigation of the Laser Sintering Process, *Int. J. Adv. Manuf. Technol.*, 2008, **38**(9–10), p 904–914. <https://doi.org/10.1007/s00170-007-1154-1>
9. K. Kempen, E. Yasa, L. Thijs, J.P. Kruth and J. Van Humbeeck, Microstructure and Mechanical Properties of Selective Laser Melted 18Ni-300 Steel, *Phys. Procedia*, 2011, **12**(Part 1), p 255–263. <https://doi.org/10.1016/j.phpro.2011.03.033>
10. J. Delgado, J. Ciurana and C.A. Rodríguez, Influence of Process Parameters on Part Quality and Mechanical Properties for DMLS and SLM with Iron-Based Materials, *Int. J. Adv. Manuf. Technol.*, 2012, **60**(5–8), p 601–610. <https://doi.org/10.1007/s00170-011-3643-5>
11. J. Sun, Y. Yang and D. Wang, Parametric Optimization of Selective Laser Melting for Forming Ti6Al4V Samples by Taguchi Method, *Opt. Laser Technol.*, 2013, **49**, p 118–124. <https://doi.org/10.1016/j.optlasotec.2012.12.002>
12. Q.B. Nguyen, D.N. Luu, S.M.L. Nai, Z. Zhu, Z. Chen and J. Wei, The Role of Powder Layer Thickness on the Quality of SLM Printed Parts, *Arch. Civ. Mech. Eng.*, 2018, **18**(3), p 948–955. <https://doi.org/10.1016/j.acme.2018.01.015>
13. ASTM International, Standard Test Methods for Density of Compacted or Sintered Powder Metallurgy (PM) Products Using Archimedes' Principle, *Astm B962-13*, 2013, **1**, p 1–7. <https://doi.org/10.1520/B0962-13.2>
14. A.B. Spierings, M. Schneider and R. Eggenberger, Comparison of Density Measurement Techniques for Additive Manufactured Metallic Parts, *Rapid Prototyp. J.*, 2011 <https://doi.org/10.1108/13552541111156504>
15. Q.B. Nguyen, M.L.S. Nai, Z. Zhu, C.N. Sun, J. Wei and W. Zhou, Characteristics of Inconel Powders for Powder-Bed Additive Manufacturing, *Engineering*, 2017 <https://doi.org/10.1016/J.ENG.2017.05.012>
16. "In718-0405 powder for additive manufacturing Process specification Powder description Nickel alloy powder," 2017. [Online]. Available: www.renishaw.com/contact
17. U. Scipioni, A.J. Wolfer, M.J. Matthews, J.R. Delplanque and J.M. Schoenung, On the limitations of Volumetric Energy Density as a design parameter for Selective Laser Melting, *JMADE*, 2017, **113**, p 331–340. <https://doi.org/10.1016/j.matdes.2016.10.037>
18. G.F. Vander Voort and E.P. Manilova, Metallographic Techniques for Superalloys, *Microsc. Microanal.*, 2004, **10**(SUPPL. 2), p 690–691. <https://doi.org/10.1017/S1431927604883442>

19. ASTM International, *Standard Test Methods for Tension Testing of Metallic Materials*. pp. 1–27
20. Keyence Corporation of America. <https://www.keyence.com/>
21. INSTRON North America. www.instron.com
22. E. Chlebus, K. Gruber, B. Kuźnicka, J. Kurzac and T. Kurzynowski, Effect of Heat Treatment on the Microstructure and Mechanical Properties of Inconel 718 Processed by Selective Laser Melting, *Mater. Sci. Eng. A*, 2015, **639**, p 647–655. <https://doi.org/10.1016/j.msea.2015.05.035>
23. W. Huang, Z. Wang, J. Yang, H. Yang, and X. Zeng, Effects of Process Parameters and Heat Treatment on the Microstructure and Mechanical Properties of Selective Laser Melted Inconel 718
24. D. Deng, R.L. Peng, H. Brodin and J. Moverare, Microstructure and Mechanical Properties of Inconel 718 Produced by Selective Laser Melting: Sample Orientation Dependence and Effects of Post Heat Treatments, *Mater. Sci. Eng. A*, 2018, **713**, p 294–306. <https://doi.org/10.1016/j.msea.2017.12.043>
25. W.M. Tucho, P. Cuvillier, A. Sjolyst-Kverneland and V. Hansen, Microstructure and Hardness Studies of Inconel 718 Manufactured by Selective Laser Melting Before and After Solution Heat Treatment, *Mater. Sci. Eng. A*, 2017, **689**, p 220–232. <https://doi.org/10.1016/j.msea.2017.02.062>
26. K. Moussaoui, W. Rubio, M. Mousseigne, T. Sultan and F. Rezai, Effects of Selective Laser Melting Additive Manufacturing Parameters of Inconel 718 on Porosity, Microstructure and Mechanical Properties, *Mater. Sci. Eng. A*, 2018 <https://doi.org/10.1016/j.msea.2018.08.037>
27. F. Caiazzo, V. Alfieri, G. Corrado and P. Argenio, Laser Powder-Bed Fusion of Inconel 718 to Manufacture Turbine Blades, *Int. J. Adv. Manuf. Technol.*, 2017, **93**(9–12), p 4023–4031. <https://doi.org/10.1007/s00170-017-0839-3>
28. Z. Wang, K. Guan, M. Gao, X. Li, X. Chen and X. Zeng, The Microstructure and Mechanical Properties of Deposited-IN718 by Selective Laser Melting, *J. Alloys Compd.*, 2012, **513**, p 518–523. <https://doi.org/10.1016/j.jallcom.2011.10.107>
29. L.M. Sochalski-Kolbus et al., Comparison of Residual Stresses in Inconel 718 Simple Parts Made by Electron Beam Melting and Direct Laser Metal Sintering, *Metall. Mater. Trans. A Phys. Metall. Mater. Sci.*, 2015, **46**(3), p 1419–1432. <https://doi.org/10.1007/s11661-014-2722-2>
30. J.P. Choi et al., Densification and Microstructural Investigation of Inconel 718 Parts Fabricated by Selective Laser Melting, *Powder Technol.*, 2017 <https://doi.org/10.1016/j.powtec.2017.01.030>
31. M. Xia, D. Gu, G. Yu, D. Dai, H. Chen and Q. Shi, Influence of Hatch Spacing on Heat and Mass Transfer, Thermodynamics and Laser Processability During Additive Manufacturing of Inconel 718 Alloy, *Int. J. Mach. Tools Manuf.*, 2016, **109**, p 147–157. <https://doi.org/10.1016/j.ijmactools.2016.07.010>
32. W. Tillmann, C. Schaak, J. Nellesen, M. Schaper, M.E. Aydinöz and K.P. Hoyer, Hot Isostatic Pressing of IN718 Components Manufactured by Selective Laser Melting, *Addit. Manuf.*, 2017, **13**, p 93–102. <https://doi.org/10.1016/j.addma.2016.11.006>
33. A. Alafaghani, A. Qattawi and M.A.G. Castañón, Effect of Manufacturing Parameters on the Microstructure and Mechanical Properties of Metal Laser Sintering Parts of Precipitate Hardenable Metals, *Int. J. Adv. Manuf. Technol.*, 2018, **99**(9–12), p 2491–2507. <https://doi.org/10.1007/s00170-018-2586-5>
34. P. Kelley, Fatigue Behavior of Direct Metal Laser Sintered (DMLS) Inconel 718, 2016
35. V.A. Popovich, E.V. Borisov, A.A. Popovich, V.S. Sufiarov, D.V. Masaylo and L. Alzina, Functionally Graded Inconel 718 Processed by Additive Manufacturing: Crystallographic Texture, Anisotropy of Microstructure and Mechanical Properties, *Mater. Des.*, 2017, **114**, p 441–449. <https://doi.org/10.1016/j.matdes.2016.10.075>
36. V.S. Sufiarov, E.V. Borisov and I.A. Polozov, Selective Laser Melting of the Inconel 718 Nickel Superalloy, *Appl. Mech. Mater.*, 2014, **698**, p 333–338. <https://doi.org/10.4028/www.scientific.net/amm.698.333>
37. K.N. Amato et al., Microstructures and Mechanical Behavior of Inconel 718 Fabricated by Selective Laser Melting, *Acta Mater.*, 2012, **60**(5), p 2229–2239. <https://doi.org/10.1016/j.actamat.2011.12.032>
38. Q. Jia and D. Gu, Selective Laser Melting Additive Manufactured Inconel 718 Superalloy Parts: High-Temperature Oxidation Property and Its Mechanisms, *Opt. Laser Technol.*, 2014, **62**, p 161–171. <https://doi.org/10.1016/j.optlastec.2014.03.008>
39. M. Sadowski, L. Ladani, W. Brindley and J. Romano, Optimizing Quality of Additively Manufactured Inconel 718 Using Powder Bed Laser Melting Process, *Addit. Manuf.*, 2016, **11**, p 60–70. <https://doi.org/10.1016/j.addma.2016.03.006>
40. P. Karimi, T. Raza, J. Andersson and L.E. Svensson, Influence of Laser Exposure Time and Point Distance on 75- μ m-Thick Layer of Selective Laser Melted Alloy 718, *Int. J. Adv. Manuf. Technol.*, 2018 <https://doi.org/10.1007/s00170-017-1019-1>
41. Y.L. Kuo, S. Horikawa and K. Kakehi, Effects of Build Direction and Heat Treatment on Creep Properties of Ni-Base Superalloy Built Up by Additive Manufacturing, *Scr. Mater.*, 2017, **129**, p 74–78. <https://doi.org/10.1016/j.scriptamat.2016.10.035>
42. Q. Jia and D. Gu, Selective Laser Melting Additive Manufacturing of Inconel 718 Superalloy Parts: Densification, Microstructure and Properties, *J. Alloys Compd.*, 2014, **585**, p 713–721. <https://doi.org/10.1016/j.jallcom.2013.09.171>

Publisher's Note Springer Nature remains neutral with regard to jurisdictional claims in published maps and institutional affiliations.